Angewandte Chemie
Eine Zeitschrift der Gesellschaft Deutscher Chemiker

Supporting Information

Diverse Nanoassemblies of Graphene Quantum Dots and Their Mineralogical Counterparts

*Zhi-bei Qu, Wei-Jie Feng, Yichun Wang, Fedor Romanenko, and Nicholas A. Kotov**

ange_201908216_sm_miscellaneous_information.pdf

Author Contributions

Z.B.Q. and W.F. designed some and performed the experiments. Z.B.Q. and Y.W. designed and conducted the computational simulations. Z.B.Q and N.A.K. wrote the paper. All the authors contributed to the writing and editing of individual sections of the manuscript. N.A.K. conceived the project and designed some of the experiments.

Supplementary Information

SUPPLEMENTARY NOTES

Statistical protocol. All of the structural parameters employed in this work were obtained after analysis of TEM images for at least 50 GQD assemblies for each sample. The lengths and diameters of GQD assemblies in TEM images were measured and analyzed by ImageJ. The fractal dimensionality values, *F,* of the structures were calculated through binary analysis of the TEM images for each sample by the means of the box-counting algorithm (Figure S8 in SI). The calculated fractal dimensionality, *F*, for each sample was employed by the arithmetic mean of at least five images for each sample.

Computational details. The density functional theory (DFT) calculations were performed using DMol3 modules in Materials Studio[1]. Generalized gradient approximation (GGA) with a Perdew-Wang 1991 (PW91) functional[2] and an all-electron double numerical basis set, augmented with a polarization *p*-function (DNP)[3] was utilized. The self-consistent field (SCF) convergence was set to 10^{-6} Ha. For geometry optimization, the convergence in energy and force were set to 10^{-5} Ha and 2×10^{-3} Ha $Å^{-1}$, respectively.

For the molecular models, a series of polycyclic aromatic hydrocarbons of different sizes were presented as GQDs without any functionalization. Then the GQDs were substituted by a number of carboxyl or hydroxyl functional groups to serve as the real GQD models in the simulation. For the GQD assemblies, the GQD dimers formed through iron-oxygen coordination bonds, were applied as the simplified models for simulations.

Geometric optimizations were performed for all of the models in the simulations while frequency analyses were used to verify that the optimized structures were at their least local minimum so no imaginary frequencies were found in those molecules. The thermodynamic properties (enthalpy, entropy, and the Gibbs free energy), FTIR, Raman spectra, and their corresponding vibration modes were calculated to GQDs and GQDs assembly models using Dmol3 analysis and frequency analysis tools.

The MD simulations were performed with Forcite Plus module in Materials Studio. The modified Dreiding forcefield[4] was applied for bonded and unbonded interactions in the models (**Table S3**). The Coulombic force was atom-based calculated with a distance cutoff of 1.55 nm. NVT ensemble was used at the ambient temperature of 298 K, controlled by the Nóse method. A time step of 1 fs was employed while the total production time was set up to 10 ns after 1 ns relaxation. A nonperiodic model was applied in the MD simulations in order to correspond to DFT calculations.

SUPPLEMENTARY DATA

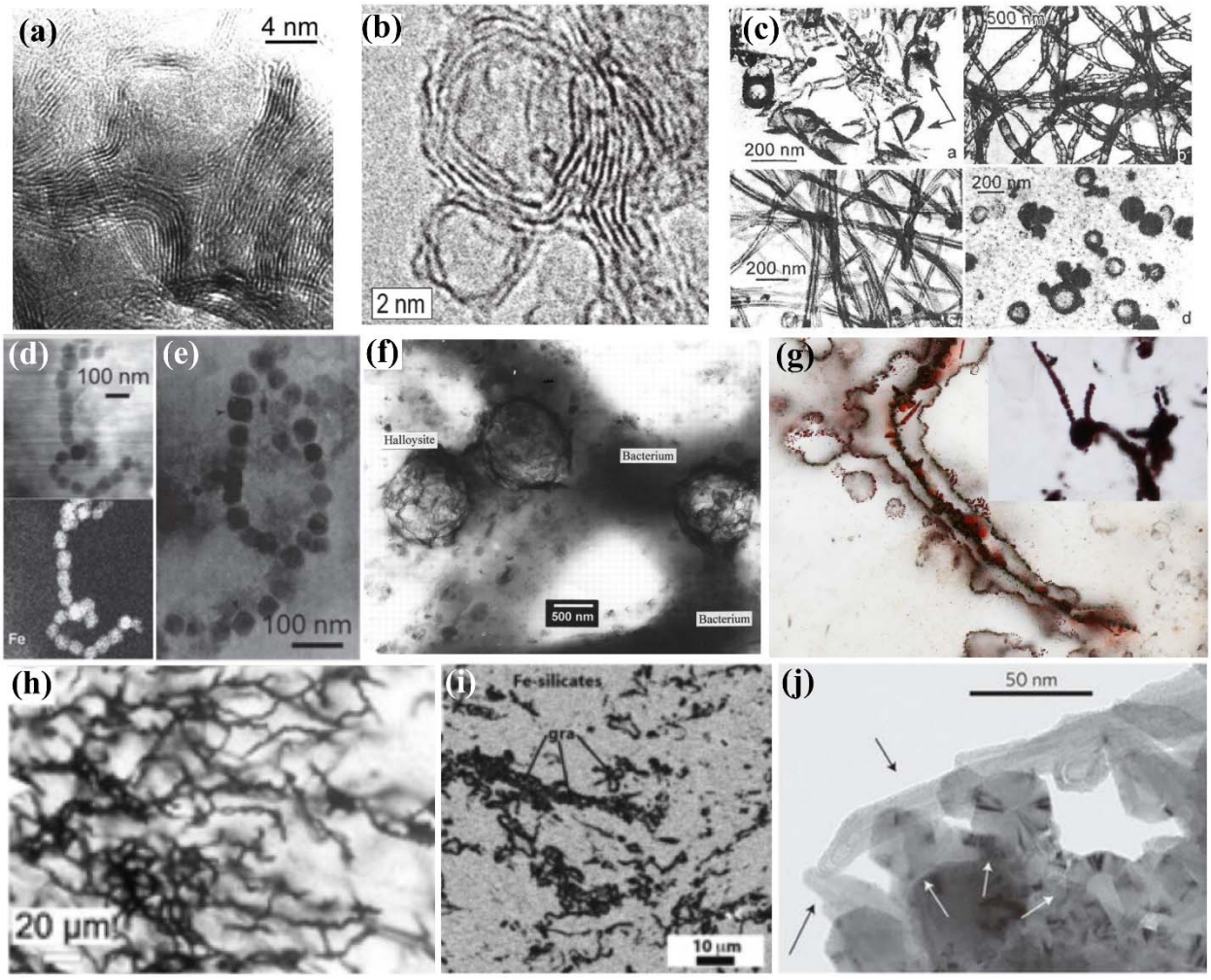

Figure S1. **Nanoshells and nanochains in minerals.** (a-b) TEM image for multi-layered shells (a) of a thin region at the edge of Zazhogino shungite rock sample,[5] approximately 2 billion years old, and (b) onion-like carbon shells observed in Allende carbonaceous chondrites.[6] (c) Hollow carbon fibers and microspheres in shungite.[7] (d-e) TEM for the magnetic nanochains in (d) Dinoflagellate[8] and (e) Sockeye salmon.[9] (f) TEM images for hollow halloysite bubbles on the surface of bacillus-type bacteria.[10] (g) Transmitted light images of haematite filaments from the Nuvvuagittuq supracrustal belt (NSB) and Løkken jaspers, microfossils of at least 3,770 million and possibly 4,280 million years old, which is the earliest form of life reported by the year 2017.[11] (h) Twisted filaments of iron oxide forming radiating networks in Ballynoe jasper, precipitation at hydrothermal vent sites back at least to the early Ordovician, 490 million years ago.[12] (i) Convoluted filaments of carbon microspheres in Fe-silicate matrix, from the approximately 3,830-million-year Akilia supracrustal belt in southwest Greenland.[13] (j) STEM image of graphite in metasediment, showing tube-like grains in the 3.7-billion-year-old metasedimentary rocks of the Isua Supracrustal Belt, Western Greenland.[14]

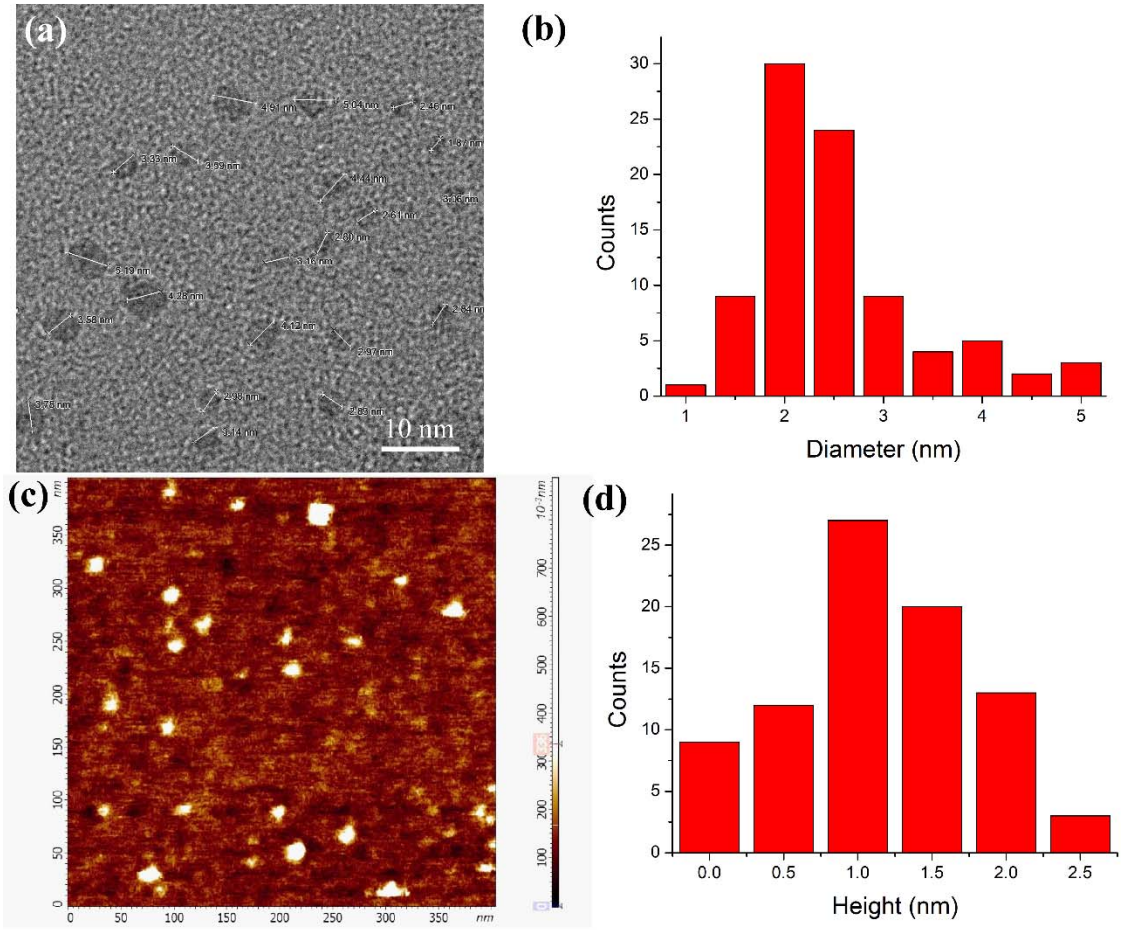

Figure S2. TEM (a) and AFM (c) images for the isolated GQDs. The statistical counts of the diameter (b) and height (d) distributions by TEM and AFM, respectively.

Comments:. Dispersity (*Đ*, aka polydispersity) is defined here and other studies[15] as standard deviation of the average diameter /average diameter. *Đ* =33.7%, 46.1% for TEM and AFM data, respectively.

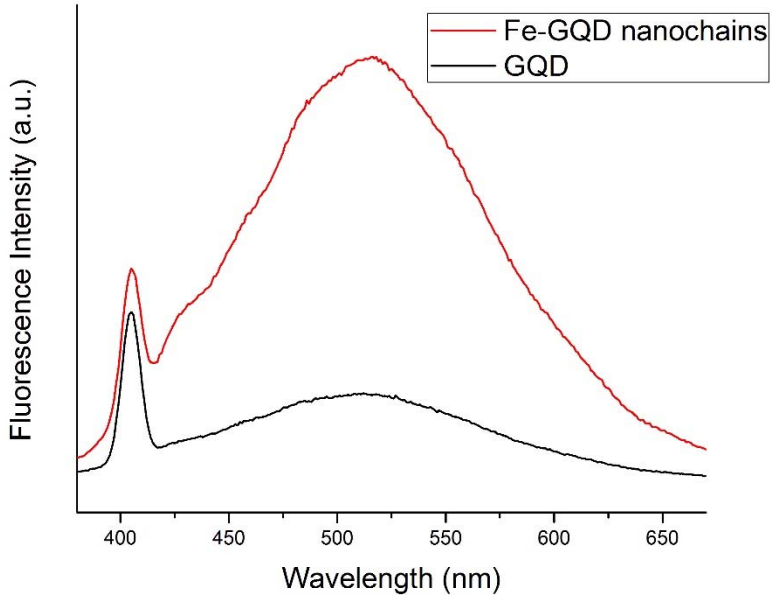

Figure S3. Fluorescent spectra for free GQD and their coordination assemblies in aqueous media for [Fe^{3+}] = 0.5 mM and [GQD] = 10 μg/mL, at pH 3.2.

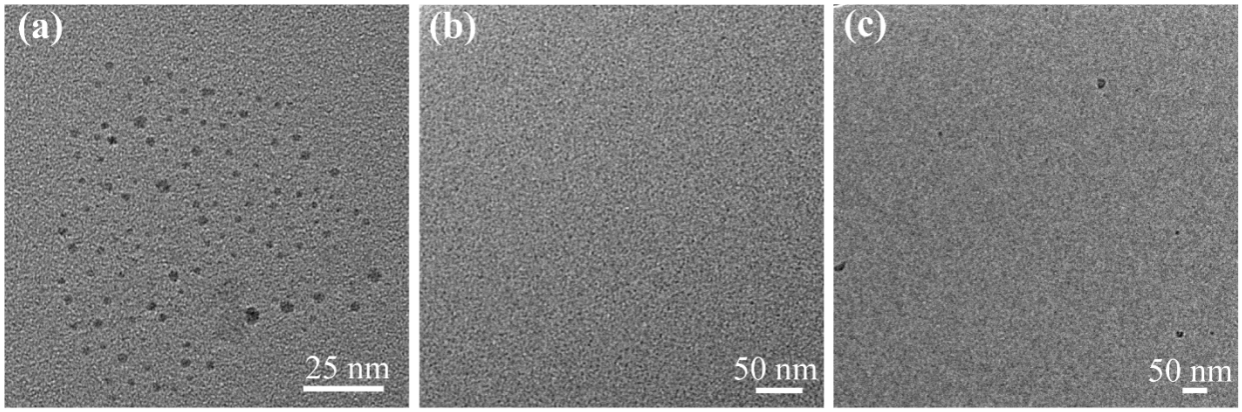

Figure S4. TEM images for the isolated GQDs in the presence of Na^+ (a), K^+ (b), and lithium ions (c). The concentration of GQDs used in the assemblies were 10 μg/mL while those for the metal ions were 0.5 mM, and pH was 3.0.

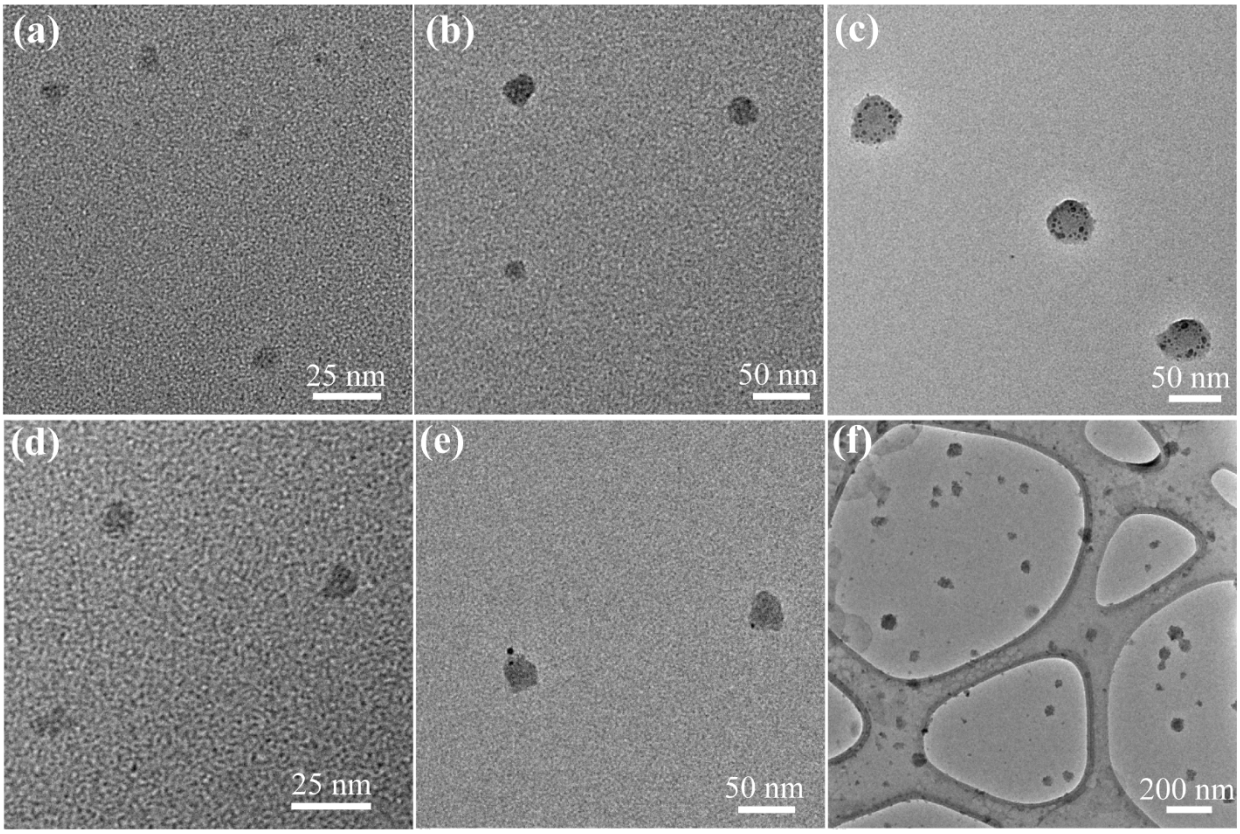

Figure S5. TEM images for the GQD assemblies in the presence of (a) Ca^{2+} ions, (b) Mg^{2+} ions, (c) Cd^{2+} ions, (d) Co^{2+} ions, (e) Mn^{2+} ions, and (f) Ni^{2+} ions. The concentration of GQDs used in the assemblies was 10 μg/mL while those for the metal ions were 0.5 mM, and pH was 3.0.

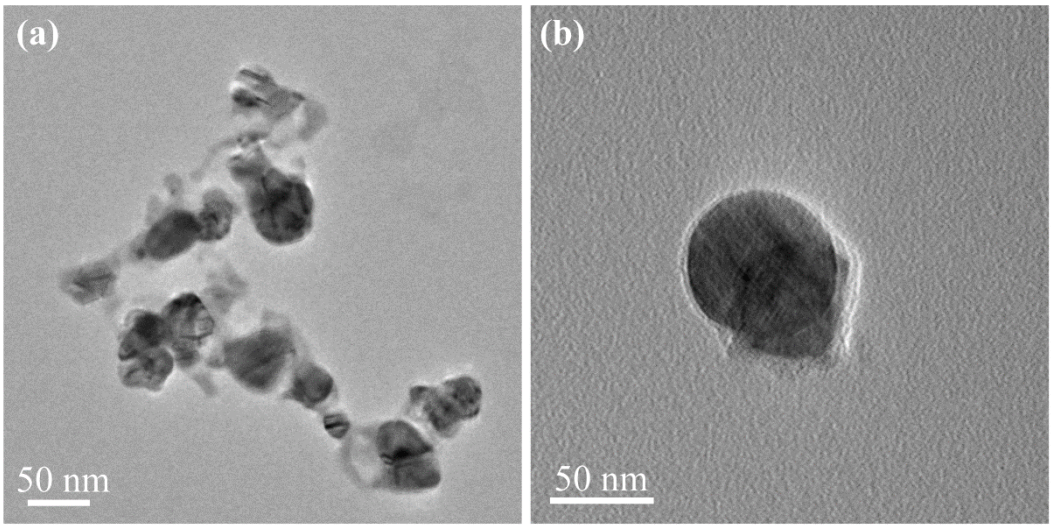

Figure S6. TEM images for the GQDs coating reduced silver NPs obtained for [Ag^{+}] = 0.5 mM and [GQD] = 10 μg/mL, at pH 3.0.

Comments: For the Ag+ ions, we observed silver nanoparticles were formed as Ag+ ions strongly hydrolyzed at the experimental conditions.

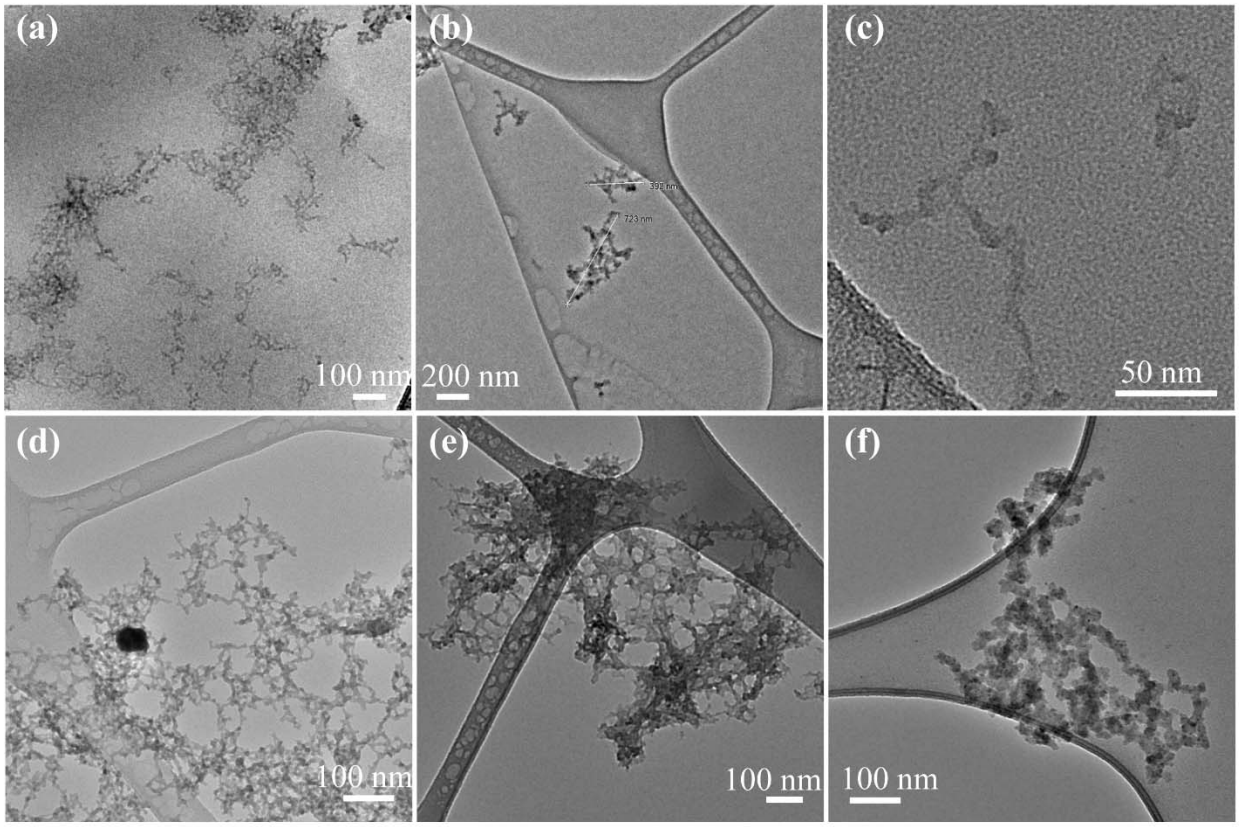

Figure S7. TEM images for the GQD assemblies in the presence of Zn^{2+} ions (a), Cu^{2+} ions (b), Cr^{3+} ions (c), Pb^{2+} ions (d), Tb^{3+} ions (e), Ce^{3+} ions (f). The concentration of GQDs used in the assemblies was 0.01 mg/mL while those for the metal ions were 0.5 mM at pH 3.0.

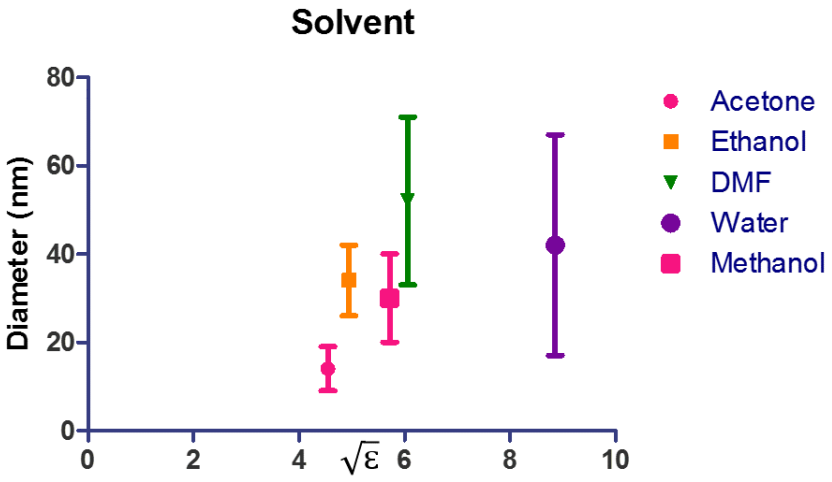

Figure S8. The dependence of the diameter (*D*) of the coordination assemblies on square root of dielectric constant of the media.

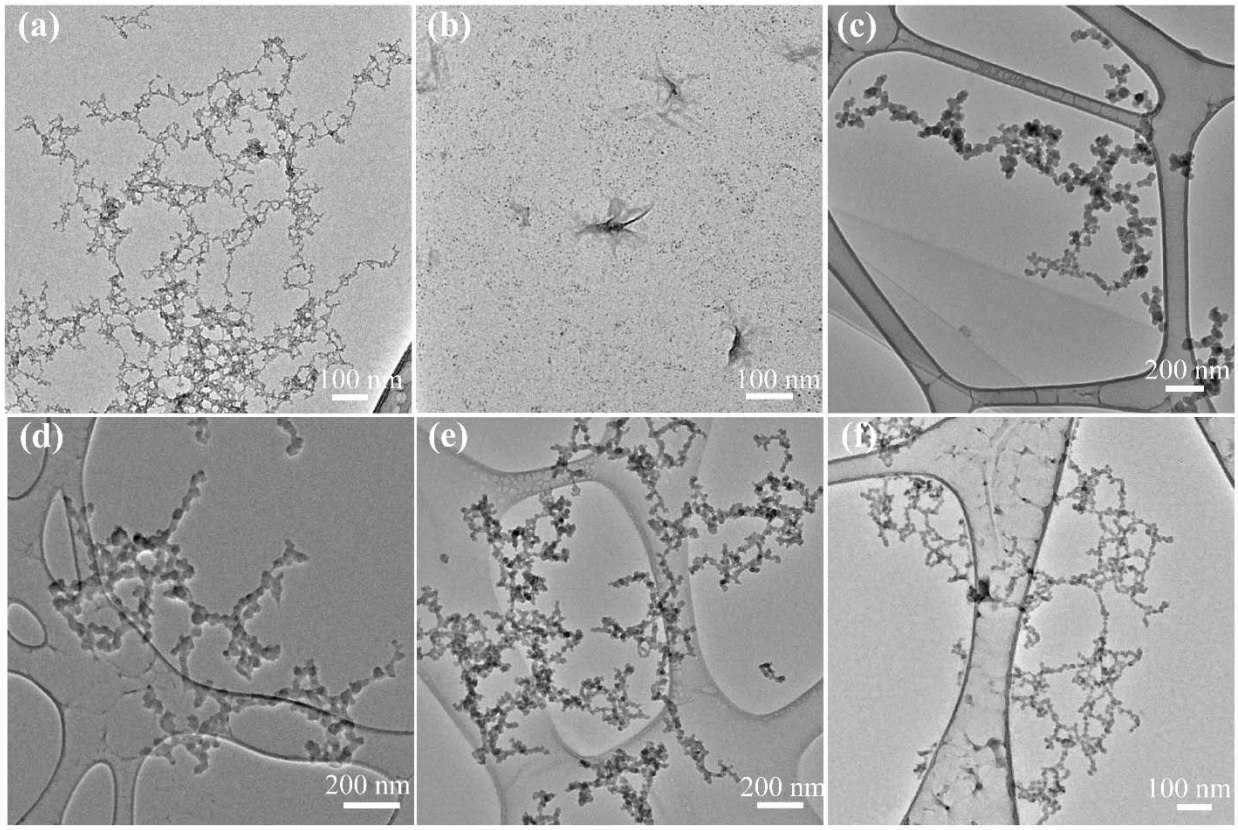

Figure S9. GQD assemblies in various solvents. TEM images for the GQD assemblies in water (**a**), DMSO (**b**), DMF (**c**), methanol (**d**), ethanol (**e**), and acetone (**f**) as solvents, respectively. The GQD assemblies were formed from 0.01 mg/mL GQD and 0.5 mM Fe^{3+}at pH 3.0 (water) for 3 h.

Comments: GQD-Fe^{3+} nanochains were observed in water, methanol, ethanol, DMF, and acetone, but in DMF (**Figure S9b**) they formed sheets. Γ does not change much in different media (**Figure 2h**). However, the width of the GQD nanochains, D, tend to be narrower in the solvent with lower dielectric constant, ε, like ethanol and acetone (**Figure S8)**, which can be rationalized by the increase of the range for electrostatic repulsion where the assembled chains ε becomes smaller.

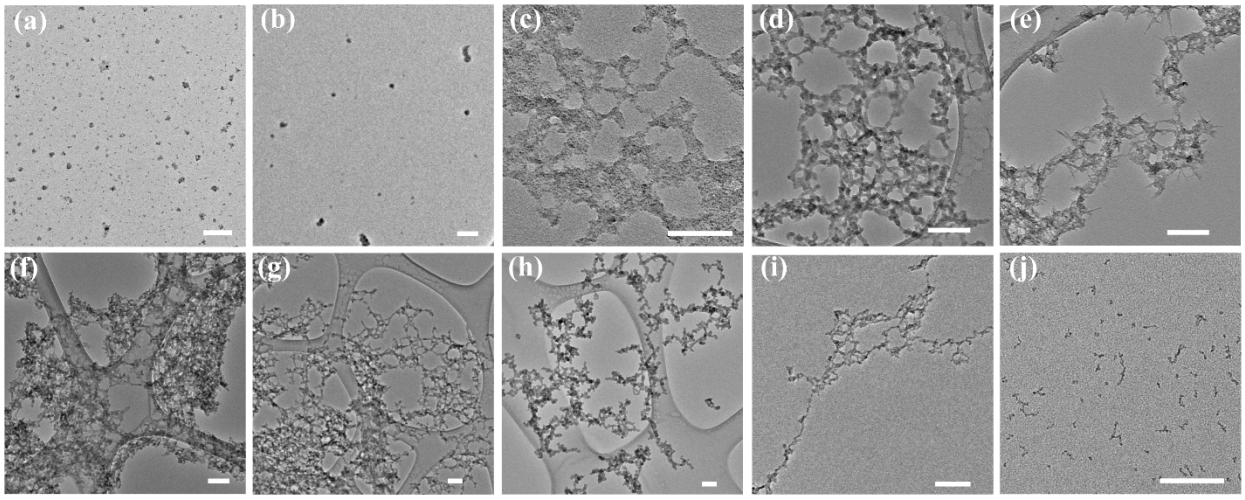

Figure S10. TEM images for Fe-GQD assemblies in various values of pH (**a-e**) and [Fe^{3+}] (**f-j**). For pH value revolution experiments, the GQD assemblies were formed from 0.01 mg/mL GQD and 0.5 mM Fe^{3+} ions under pH 1.5 (a), pH 2.0 (b), pH 2.5 (c), pH 3.0 (d) and pH 3.5 (e), respectively. For Fe^{3+} concentration revolution, the GQD assemblies were produced from 0.01 mg/mL GQD and Fe^{3+} solution in concentration of 50 μM (f), 100 μM (g), 200 μM (h), 500 μM (i) and 1 mM (j), respectively. Whereas the pH value was controlled to 3.2 in the latter experiments. Scale bars in all the images is 100 nm.

Comments: The pH value affects the hydration state of Fe^{3+} ions and ionization of GQDs. We investigated the different assemblies for 0.01 mg/mL GQD and 0.5 mM Fe^{3+} in a pH range between 1.5 and 3.5 (**Figure S10 a-e**). Fe^{3+} ions are coordinated with OH^- groups at pH above 4. Concomitantly, for the values of pH below 1, the carboxyl groups of GQDs are protonated, which is expected to inhibit the ability of carboxyl groups to coordinate Fe^{3+}. Correspondingly, the largest Γ for coordination assemblies of GQDs are expected in the pH range between 1.5 and 3.5.

At pH from 1.5 to 2, no GQD assemblies were observed. At pH 1.5, isolated GQDs without obvious organizational patterns were found. For pH 2.5 and 3, an interconnected network of nanochains with a great number of cross-points between the chain branches formed. The average vertex valency (V) from graph theory was employed to describe the cross-linking complexity of the nanochains (**Figure S11**). V increased from 2.7 to 3.0 when pH value rises from 2.5 to 3.0. Nanochains formed at pH 3 showed lower distribution in diameter and a better-defined boundary

than those at pH 2.5. For the pH 3.5 sample, networks of GQD assemblies with star-like assemblies were observed, which reflect the interplay between GQD coordination and the hydrolysis of iron ions (**Figure 2f**). Overall, it is demonstrated that coordination assemblies of GQDs induced by Fe^{3+} ions at pH 3.2 display the largest Γ of 2400 ± 900 nm (**Figure S12**).

We investigated the different assembly behavior for 0.01 mg/mL GQD and Fe^{3+} ions of the concentrations in a range between 50 uM and 1 mM at pH 3.2 (**Figure S10 f-j**). The values of Γ and D, and their interconnectivity, V, change greatly for different [Fe^{3+}]. For the samples with [Fe^{3+}] < 200 uM, network assemblies of high level of cross-linking ($V \geq 3.5$) were formed while nanochains with D =7 ± 3 nm were formed when [Fe^{+3}] concentration was higher than 500 μM.

The interconnectivity of the GQD chains can also be quantified using the fractal dimensionality (F) of the structures (**Figure S13**) that can be used as a quantitative measure describing the assembly pattern. $F \sim 2$ means that the assembled structure can be described as a 2D material; $F \sim 2$ means that it is more likely to be a structure with a linear assembly pattern with fewer constructive features such as cross-linking. The fractal dimensionalities (F) were 2.01, 1.90, 1.70, 1.53, and 1.45 for the GQD assemblies from 0.01 mg/mL GQD and Fe^{3+} solution in concentration of 50 μM, 100 μM, 200 μM, 500 μM, and 1 mM, respectively. It is concluded that the fractal dimensionality decreased when the concentration of Fe^{3+} ions increased. Statistical analysis of D and Γ shows that that the GQD assemblies tend to be shorter and thinner nanochains as [Fe^{3+}] increases. For the Fe-GQD nanochains with 1 mM iron ions (**Figure S10j**), the diameters of the nanochains were observed to be as small as 5 nm, which is close to the size for single GQDs (2-4 nm in diameter).

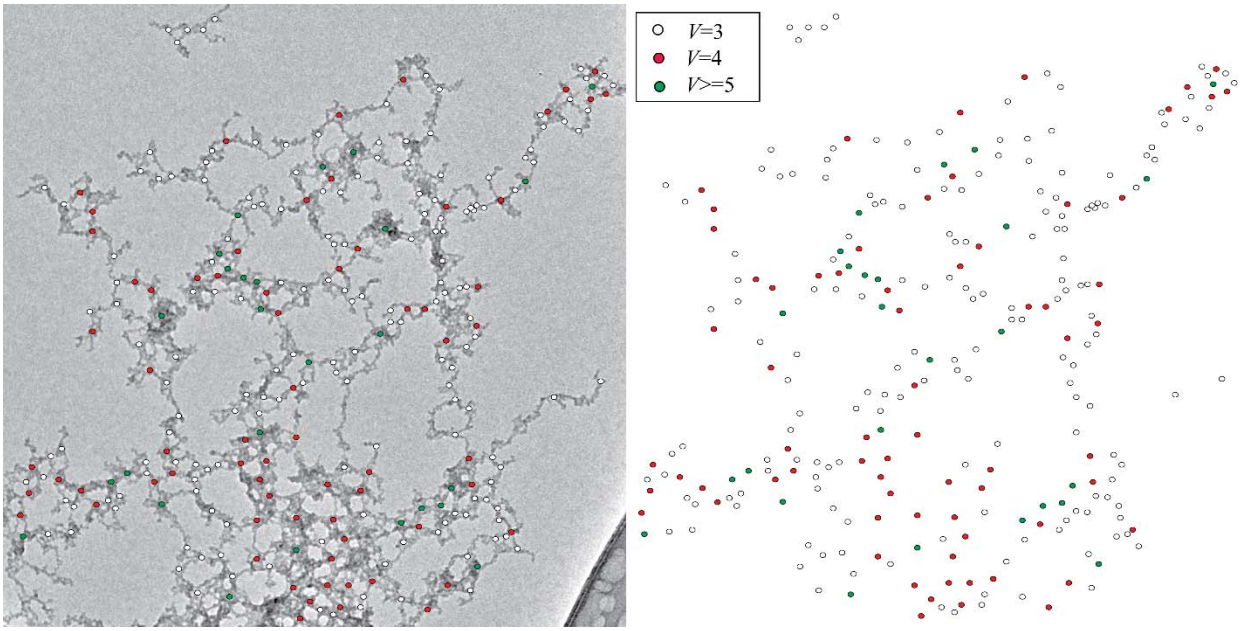

Figure S11. The average vertex valency (V) of Fe-GQD nanochains.

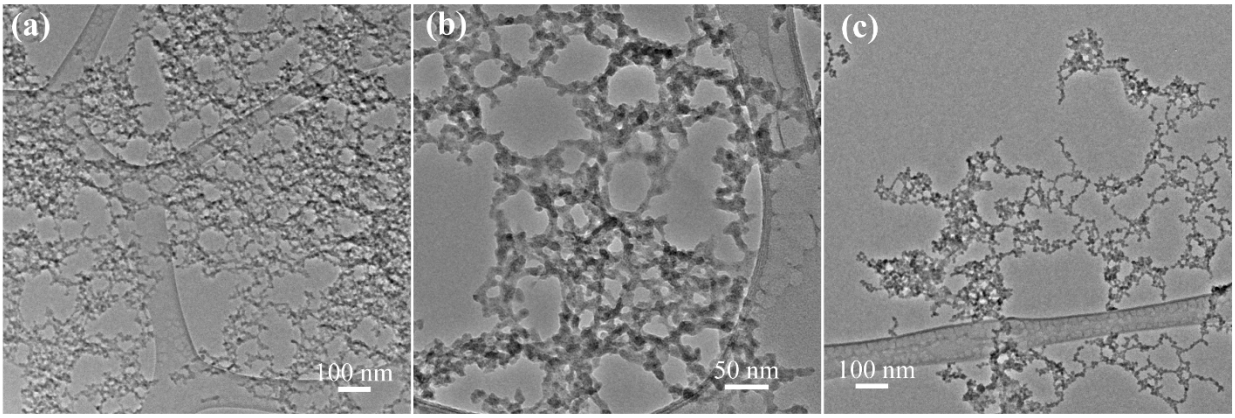

Figure S12. TEM images for Fe-GQD assemblies at various pH values. The GQD assemblies were formed from 10 μg/mL GQD and 0.5 mM Fe^{3+} ions under pH 2.8 (a), pH 3.0 (b), and pH 3.2 (c).

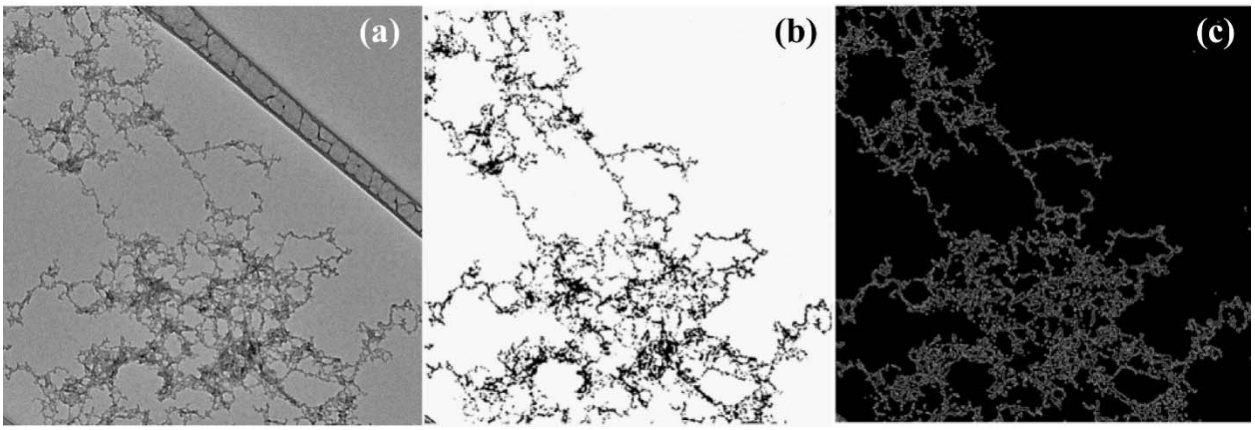

Figure S13. TEM image (a), images after filtering, noise reduction, and binarization (b), edge detection (c) for box counting algorithm of fractal dimension calculation of Fe-GQDs nanochains.

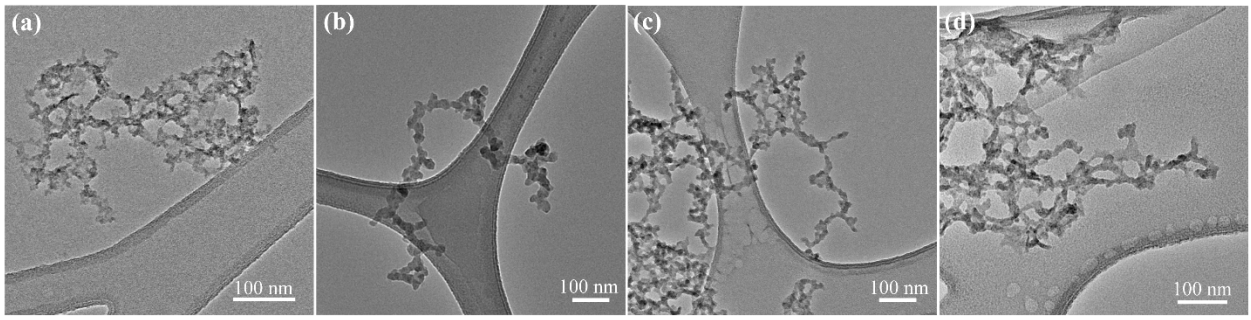

Figure S14. TEM images for Fe-GQD assemblies in various GQD concentrations. The GQD assemblies were induced by 0.5 mM Fe^{3+} ions at pH 3.2 with 1 μg/mL (a), 10 μg/mL, (b), 50 μg/mL, and 100 μg/mL GQD.

Comments: The coordination assemblies of GQDs did not show obvious change either in morphology or geometrical parameters of Fe-GQD nanochains for different concentrations of GQDs in the range from 1 μg/mL to 100 μg/mL (**Figure S13**). Chemical element analysis of the GQDs carried out by X-ray photoelectron spectroscopy (XPS) indicated that the atomic ratio of C:O was 1.89 (Table S1). An ideal GQD 'molecule' 2 nm in diameter and single layer of graphene would contain 96 carbon atoms for the molecular skeleton. Therefore, $C_{96}O_{50.8}$ will be the averaged chemical formula for GQD with a molecular weight of 1965 Da. Thus, the [GQD] was between 0.5 and 50 μM, which is remarkably lower than $[Fe^{+3}]$ = 0.5 mM used in these experimental series. Thus, [GQD] only affected the yield of the GQD assembled nanochains but did not affect the morphology and size as it can be regard as isolated GQDs far away from each other in low concentration.

Table S1. Atomic concentration of each elements from XPS mapping.

Sample	C [%]	O [%]	N [%]	Fe [%]
GQD	64.4	34.1	1.5	--
Fe-GQD nanochains	62.5	36.0	1.0	0.53

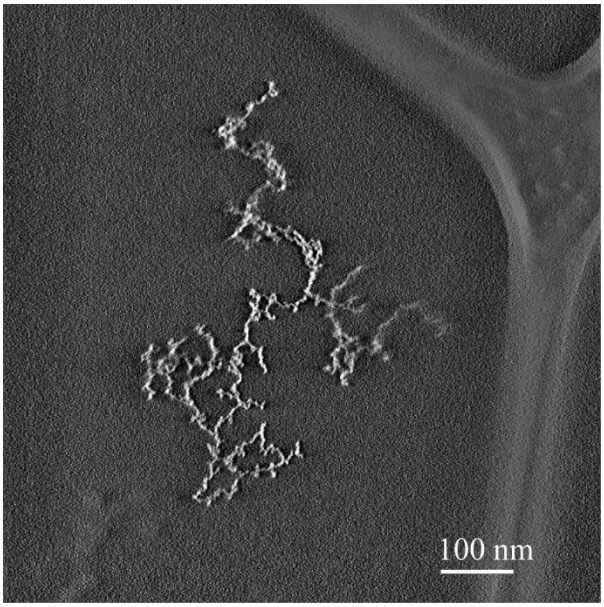

Figure S15. Cross-section images for Fe-GQD nanochains from STEM tomographic reconstruction. The Fe-GQD nanochains were assembled at 10 μg/mL GQD and 0.5 mM Fe^{3+} ions under pH 3.2.

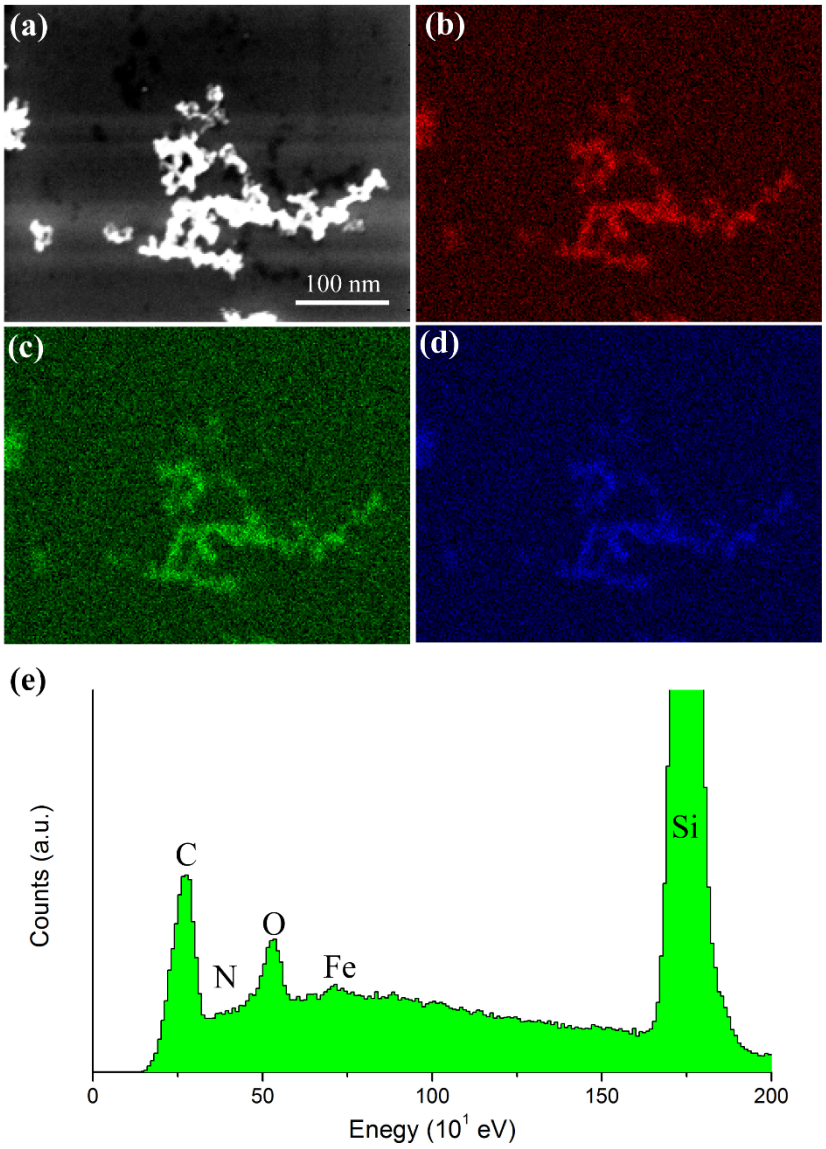

Figure S16. SEM image of Fe-GQD nanochains (a) and elemental mapping using C Kα (b), O Kα (c), Fe Lα (d). EDAX spectrum of Fe-GQD nanochains (e). The Fe-GQD nanochains were fabricated at [Fe^{3+}] = 0.5 mM, [GQD] = 10 µg/mL, and pH 3.2.

Comments: The elemental analysis showed a similar result, except that nitrogen was not detected. EDAX element mapping demonstrated that carbon, oxygen, and iron were observed only where Fe-GQD nanochain is present.

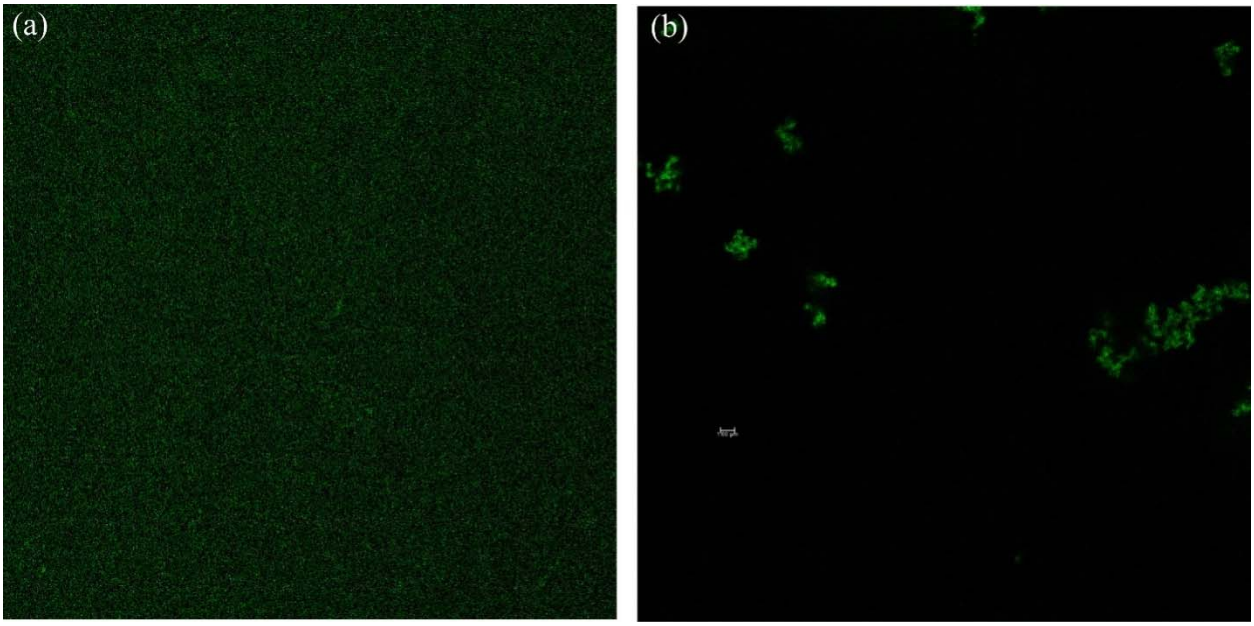

Figure S17. Confocal fluorescence images for free GQDs (a) and Fe-GQD nanochains assembled at [Fe^{3+}] = 0.5 mM and [GQD] = 10 μg/mL, under pH 3.2 for 3 min (b). The side of the square scanning area is 80 micrometer.

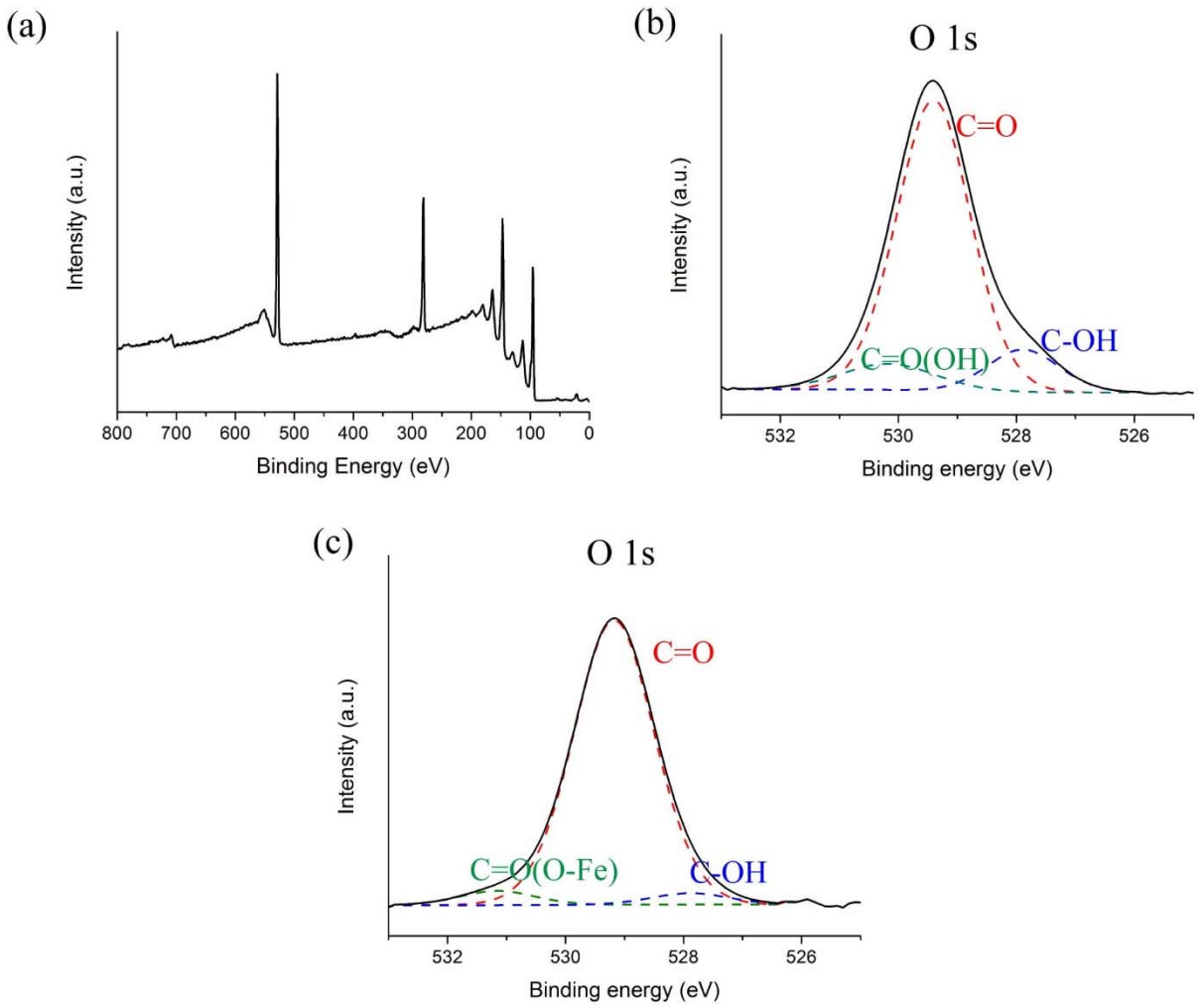

Figure S18. XPS survey spectrum for Fe-GQD nanochains (a). High resolution XPS O 1s spectra for GQDs (b) and Fe-GQD nanochains (c). The Fe-GQD nanochains were fabricated at [Fe^{3+}] = 0.5 mM, [GQD] = 10 μg/mL, and pH = 3.2.

Comments: The high-resolution Fe 2*p* XPS spectra showed that $FeCl_3$ solution without GQDs showed a three-component peak, corresponding to the coordination environment of the centered iron ions with Fe-Cl, Fe-H_2O and Fe-O bonds. After the formation of Fe-GQD nanochains, the Fe 2*p* XPS peak showed a redshift from 711.2 eV to 710.5 eV, reflecting the change of coordination condition for Fe^{3+} ions during the assembly process. The Fe 2*p* XPS peak for Fe-GQD nanochains is also consisting of three components, those are coordination bonds between iron ion and water

molecules, carboxyl groups and a small amount of hydroxyl groups on GQDs. Similar results were drawn from Gaussian fitting of O 1*s* peak that the oxygen in either GQDs or Fe-GQD nanochains were composed from three components. Those are C=O oxygen from ketone groups, C=O-(OH) carbonyl oxygen from the carboxyl groups and C-OH oxygen from hydroxyl groups. After the formation of Fe-GQD nanochains, the C=O oxygen, C-OH oxygen peaks remained at the same position as that for GQDs. However, the C=O-(OH) carbonyl oxygen peak showed a notable shift to higher binding energy from 530.0 eV to 531.2 eV. The blue shift of carbonyl oxygen on carboxyl groups 1*s* peak reflected in the change in chemical environment of carboxyl groups after the formation of Fe-GQD nanochains. More specifically, the coordination bonds between iron ions and carboxyl groups are strongly polarized, resulting in the charge transfer from $–COO^-$ to Fe^{3+}. That is why the C=O-(OH) carbonyl oxygen peak showed a blue shift to higher binding energy after coordination bonding to iron in Fe-GQD nanochains and also a redshift in Fe 2*p* peak.

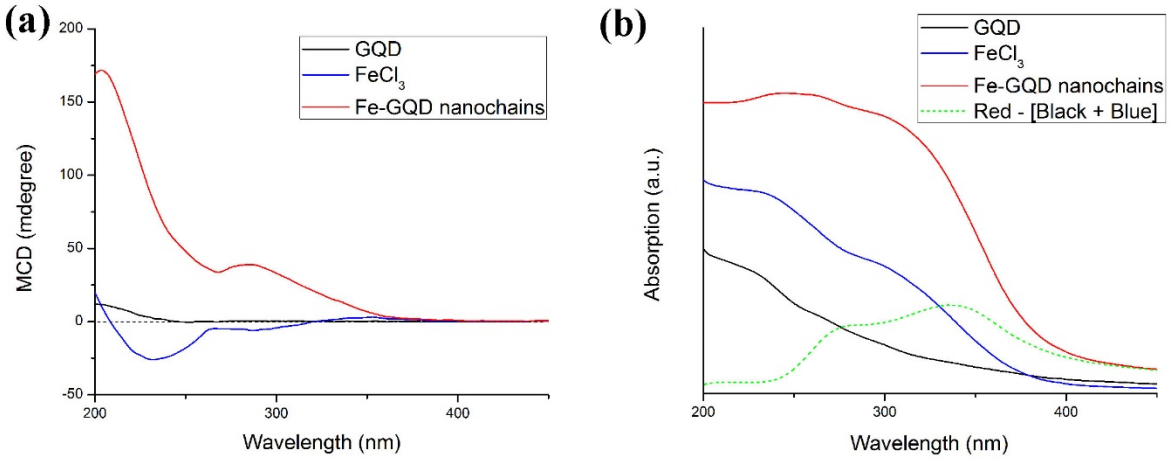

Figure S19. MCD (**a**) and UV-Vis (**b**) spectra for GQD, iron (III) chloride solution, and Fe-GQD nanochains. The Fe-GQD nanochains were fabricated at [Fe^{3+}] = 0.5 mM, [GQD] = 10 μg/mL, and pH 3.2.

Comments: The UV-Vis spectra showed no obvious change in peak wavelength after the formation of Fe-GQD nanochains. This is because the UV-Vis absorption peaks of GQDs and iron ions overlay greatly in UV region with a similar shoulder peak around 260 nm. Moreover, carboxyl groups and water molecules showed a similar splitting energy change for coordination bonding in the spectrochemical series of ligands. In order to study the interaction of iron ions and GQDs, the subtraction of spectra for GQD and iron chloride solutions from that for Fe-GQD nanochains with the same concentrations of iron ions and GQDs was plotted in **Figure S19d** (green dash line). Two peaks at 280 nm and 345 nm, respectively, were shown in the subtraction plot, which corresponds well to the typical absorption of Fe(III)-carboxylic acid compounds.[16]More details were revealed from the MCD spectra. The MCD showed a remarkable enhancement of absorption intensity (15 times) at 210 nm after the formation of Fe-GQD nanochains. For the aqueous solution of Fe^{+3}, two negative peaks and one positive peak were found by MCD. The negative peaks are from $^2T_{2g}$ - $^2T_{2u}$ transition while the positive peak is attributed to $^2T_{2g}$ - $^2T_{1u}$. After the formation of Fe-GQD

nanochains, only positive peaks were found, which implies that the $^2T_{2g}$ - $^2T_{1u}$ transition dominates in the charge transfer based absorption. It corresponds very well to the result that the ligands transfer from water molecule to GQDs. The t_{1u} orbital mainly consisted of the π orbital of the ligands. GQDs have large aromatic cyclic systems, so it is easily understood that the $^2T_{2g}$ - $^2T_{1u}$ transition was largely enhanced. To further illustrate this, MCD measurements under different temperatures were done (**Figure S20**). The results showed that the MCD peak around 300 nm increased at lower temperature, and vice versa. It shows clearly that the MCD signal of Fe-GQD nanochains are mainly from *C* term, which only exists in paramagnetic material with multiple spin states. It is consistent with the semi-full $3d^5$ orbital of iron ion with sextet spin multipilicity. It is notable that the Fe-GQD nanochains showed different MCD signals with opposite magnetic field directions (**Figure S21**), indicating the magnetic coupling between iron atoms in the Fe-GQD nanochains.

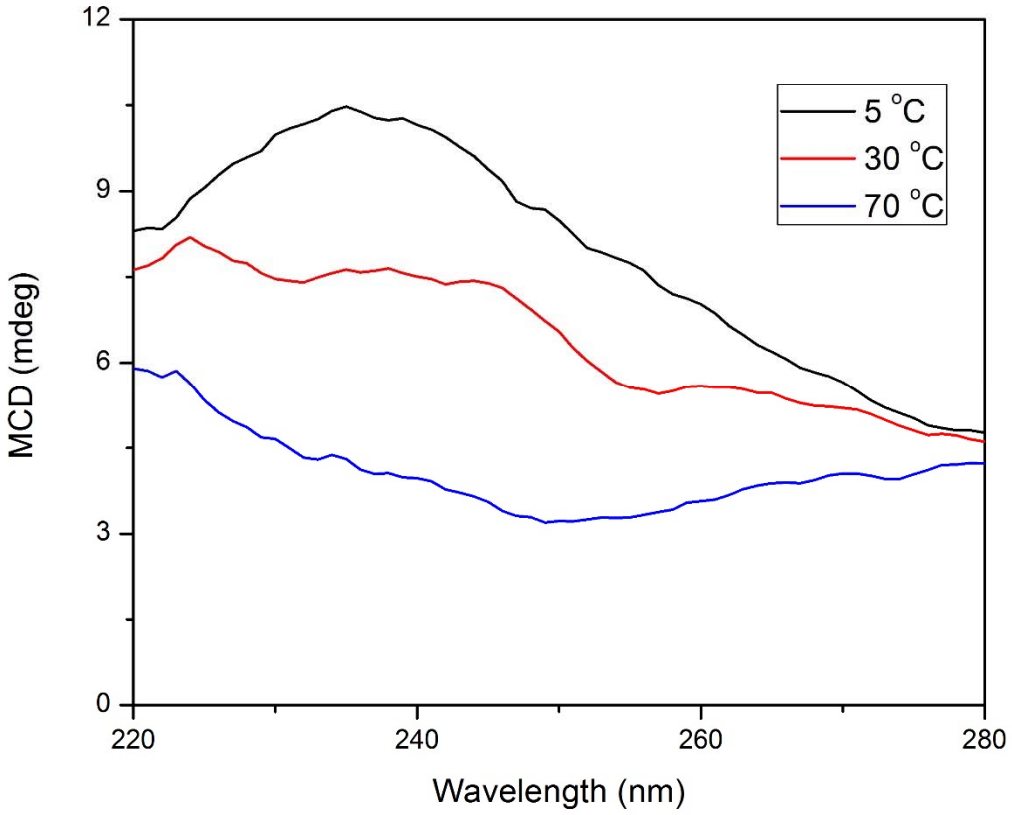

Figure S20. MCD spectra Fe-GQD nanochains at different temperatures. The Fe-GQD nanochains were fabricated at [Fe^{3+}] = 0.5 mM, [GQD] = 10 μg/mL, and pH 3.2.

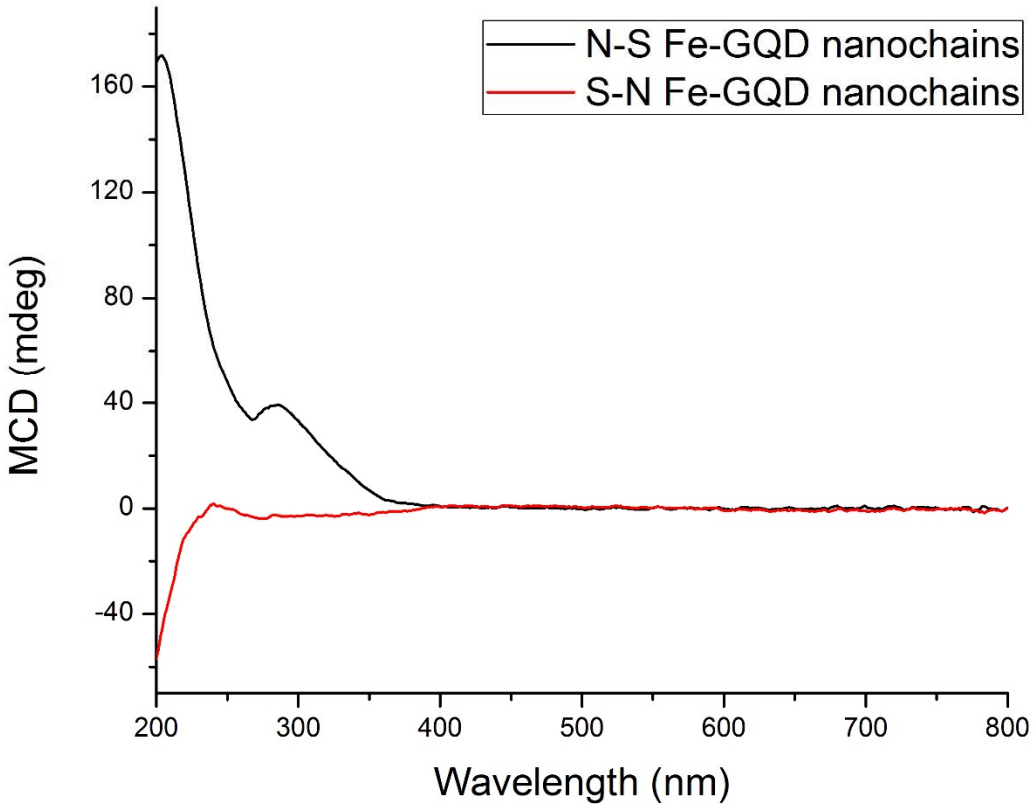

Figure S21. MCD spectra Fe-GQD nanochains for magnetic fields with opposite directions. The Fe-GQD nanochains were fabricated at [Fe^{3+}] = 0.5 mM, [GQD] = 10 μg/mL, and pH 3.2.

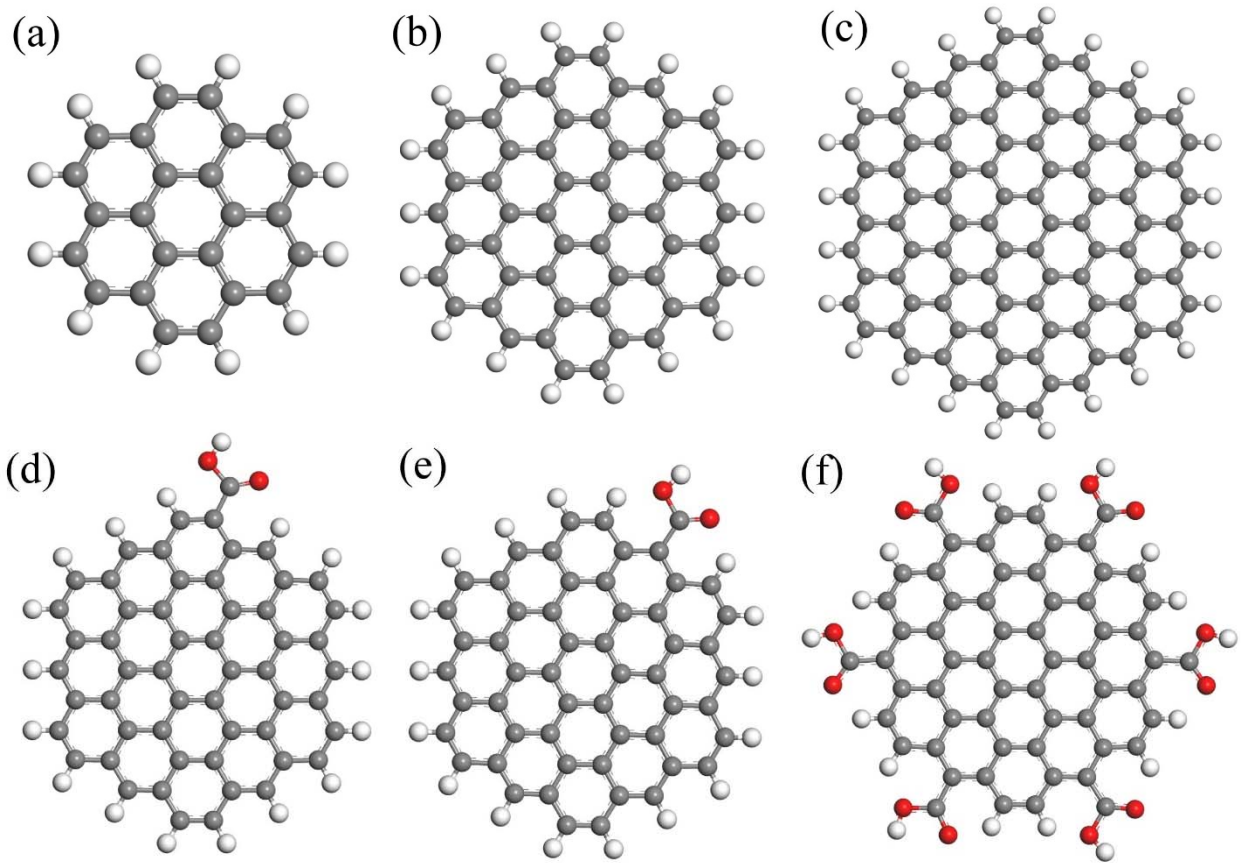

Figure S22. Optimized structural configurations for (a) 2x2, (b) 3x3, (c) 4x4, and 3x3 GQDs with (d) -COOH at corner, (e) -COOH at side edge, (f) six -COOH groups at all side edges.

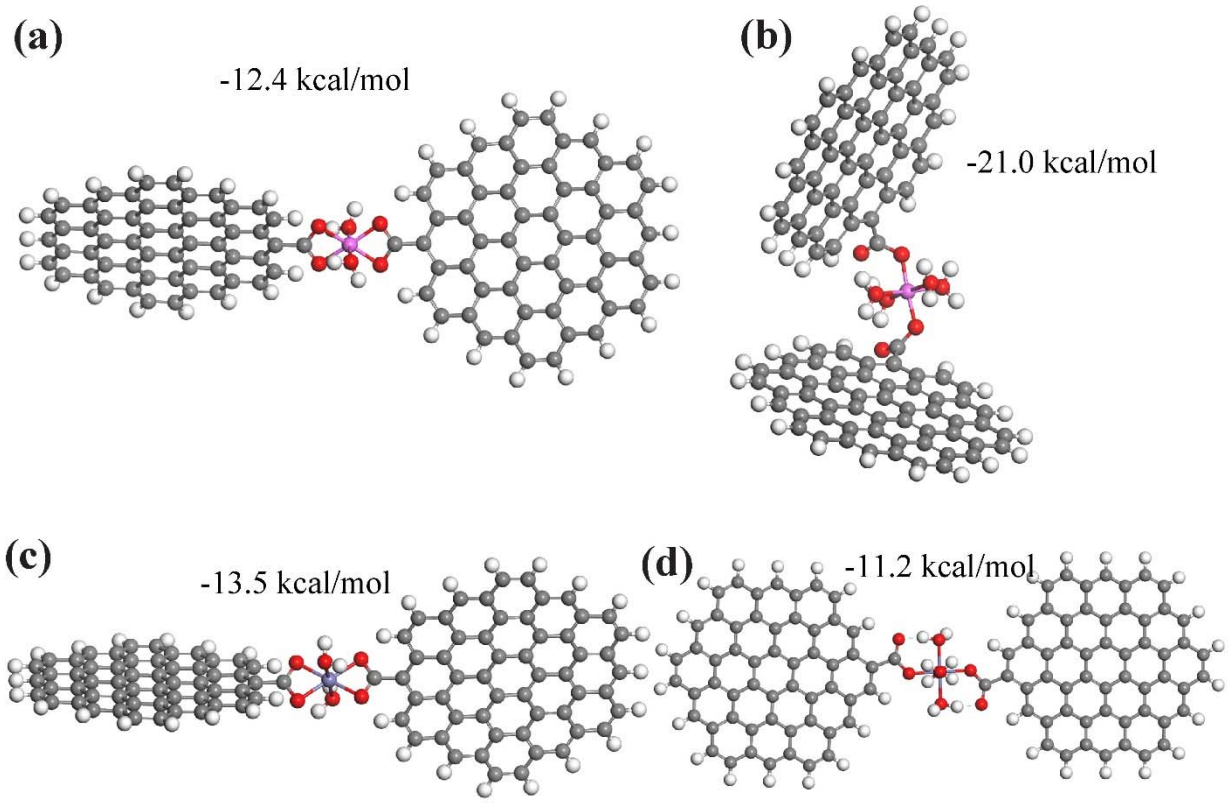

Figure S23. Optimized structural configurations and reaction heat, ΔH, for (a) bidentate, (b) monodentate Al-GQD assemblies, (c) bidentate, and (d) monodentate Fe-GQD assemblies.

Comments: The reaction heat was calculated by the following method.

$$\Delta H = \sum E_{binding}^{product} - \sum E_{binding}^{reagent} \qquad (1)$$

Where E_{binding} is the binding energy of each molecule from DFT calculations. The reaction formula was:

$$2\ \text{GQD} + \text{M(H}_2\text{O)}_6^{3+} \rightarrow \text{M(GQD)}_2\,\text{(H}_2\text{O)}_{6-n}^{3+} + n\ \text{H}_2\text{O} \qquad (2),$$

where $n = 2$ for monodentate and $n = 4$ for bidentate coordination assemblies. M = Al^{3+} or Fe^{3+} ions for Al-GQD assemblies and Fe-GQD assemblies, respectively.

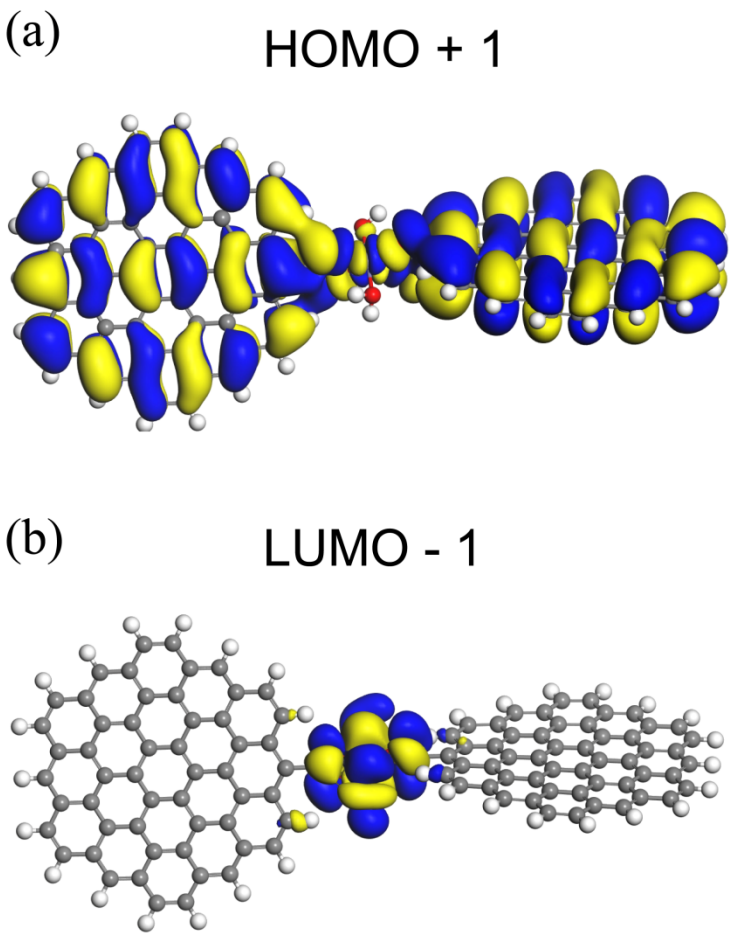

Figure S24. Molecular orbitals for bidentate GQD-Fe-GQD assemblies: (a) HOMO+1, and (b) LUMO-1. The isovalue was set to be 0.15 eV. Color coding: gray - carbon, red - oxygen; white - hydrogen; blue - iron; pink - aluminum. Blue solid - positive orbital; yellow solid -negative orbital.

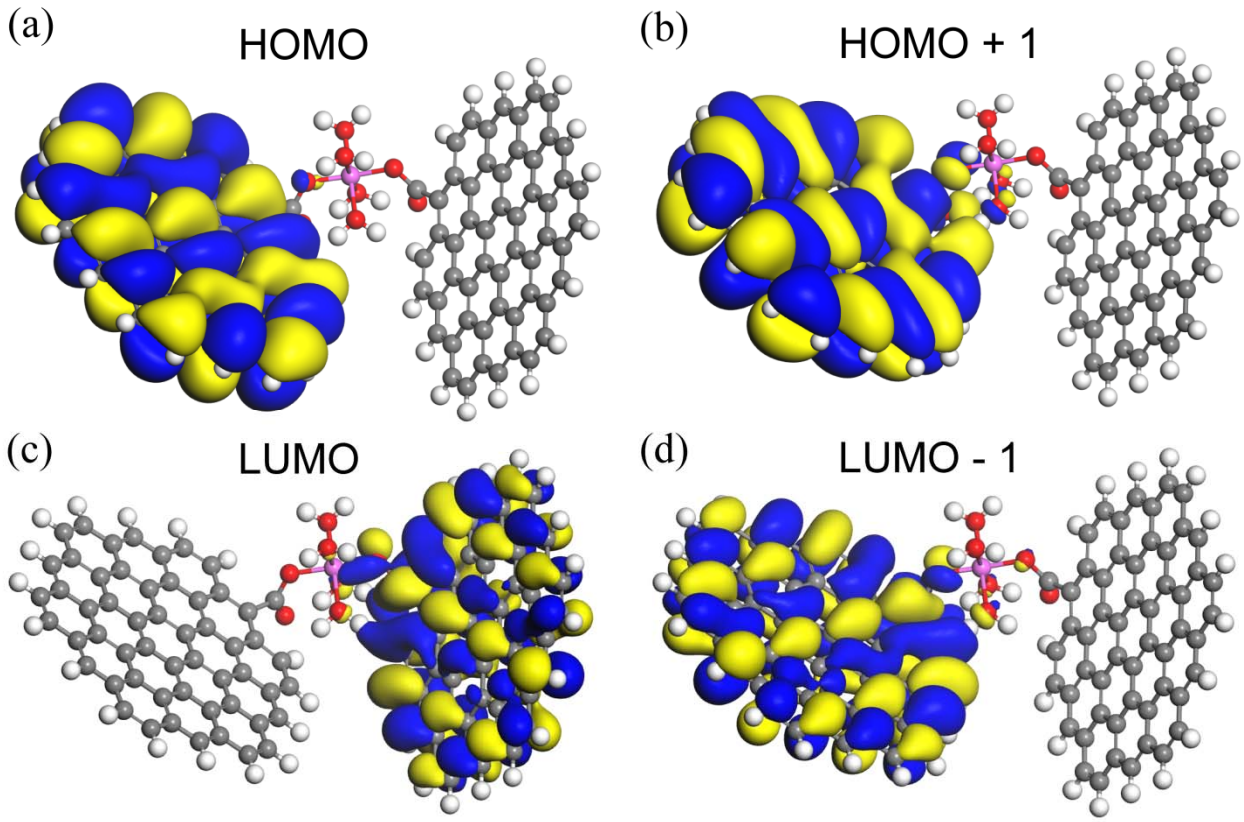

Figure S25. Molecular orbitals for monodentate GQD-Al-GQD assemblies: (a) HOMO, (b) HOMO+1, (c) LUMO and (d) LUMO-1. The isovalue was set to be 0.15 eV. Color coding: gray – carbon; red - oxygen; white - hydrogen; blue - iron; pink - aluminum. Blue solid for positive orbital and yellow solid for negative solid.

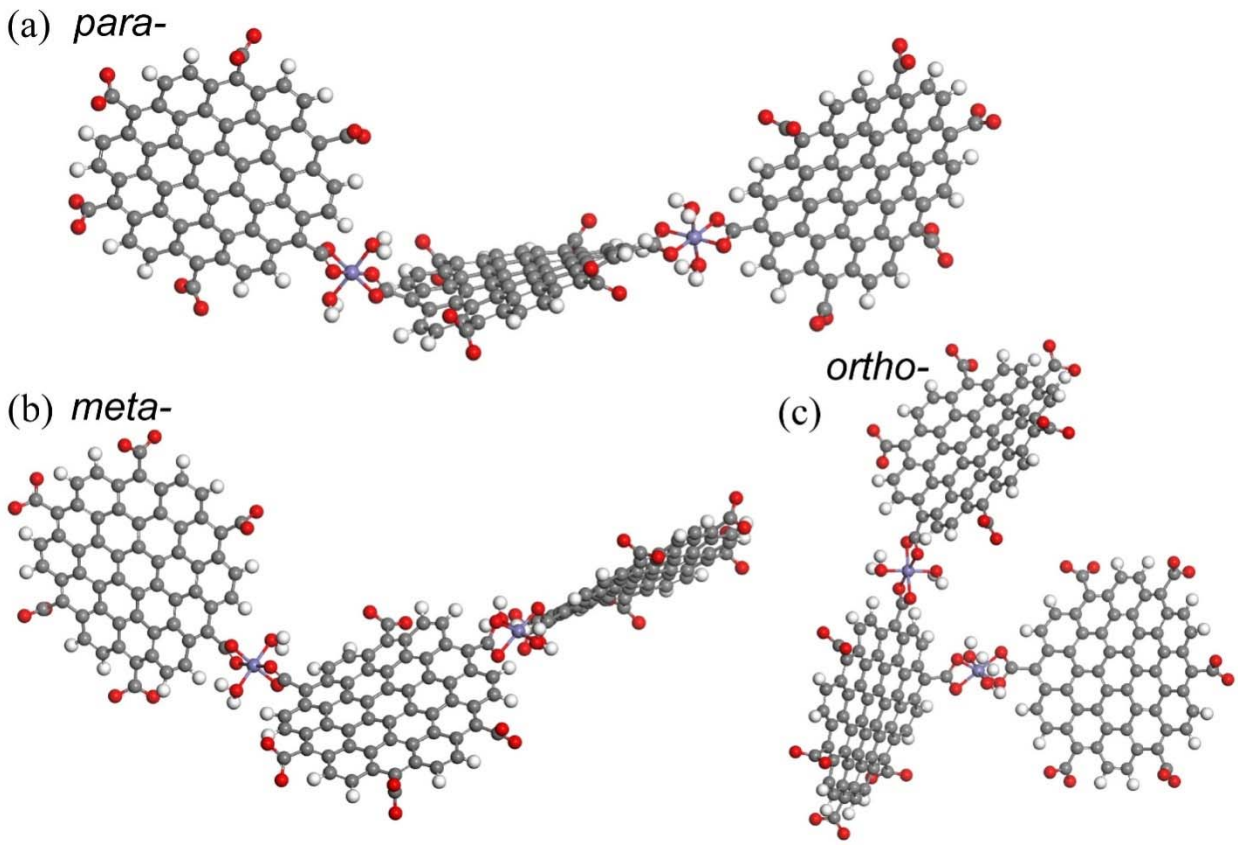

Figure S26. Optimized structural configurations for (a) *para*-, (b) *meta*- and (c) ortho-coordinated Fe-GQD trimers.

Comments: The tetrahedral geometry of the bridge displays a dihedral ligand-metal-ligand angle of 70 degrees, which made the metal-GQD assemblies in angled shapes. When the metal-GQD dimers grow up to trimers, the second coordination "bridge" could be formed in various sites if the GQDs had multiple carboxyl groups. Therefore, a series of metal-GQD assembled trimers with *para*-, *meta*- and *ortho*- configurations were investigated (**Figure S26** and **S27**). It can be concluded that for either Al^{3+} or Fe^{3+}, the *para*- type trimers are the most stable ones from an energy level as the *para*- assemblies provide the smallest electrostatic repulsion and steric effect. Moreover, the energy difference between the *meta*-, *ortho*- Fe-GQD trimers and the *para*- ones are 17.5 and 24.3 kcal/mol, respectively. Their aluminum counterparts showed much smaller energy

differences which are 9.4 and 11.7 kcal/mol, respectively. It can be inferred on the basis of thermodynamics that the Fe-GQD trimers are more favorable in *para*- type while the Al-GQDs hold higher possibilities in *meta*- and *ortho*- types than their Fe consisting counterparts. The diversity of Al-GQDs in possible configurations in various sites also helps in the isotropy of the Al-GQD assemblies, resulting in the formation of supraparticles. In addition to total energies, the Coulomb energies of the systems were calculated. Similarly, the Al-GQD trimers showed relatively smaller energy differences in Coulomb potential for *para*-, *meta*- and *ortho*- isomers than those for Fe-GQD assemblies (**Table S2**). From an electrostatic aspect, the Al-GQD trimers showed no obvious bias for all constructional isomers while Fe-GQD trimers would favor in *para*- and *meta*- configurations rather than *ortho*- ones. The Fe-GQD trimers exhibited a quasi-linear fashion for either *para*- or *meta*- configurations (**Figure S20**), corresponding to the 1D nanochains shape of Fe-GQD assemblies.

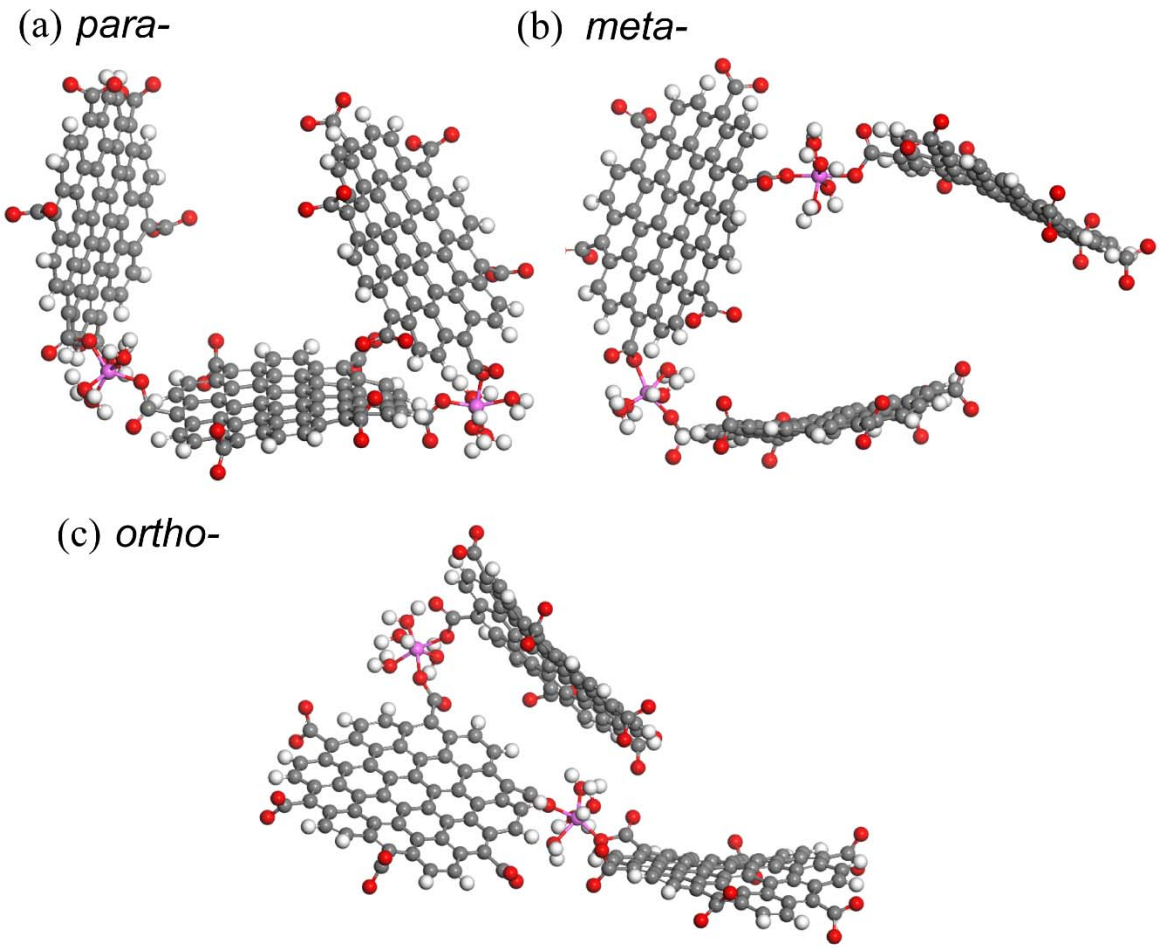

Figure S27. Optimized structural configurations for (a) *para*-, (b) *meta*- and (c) ortho-coordinated Al-GQD trimers.

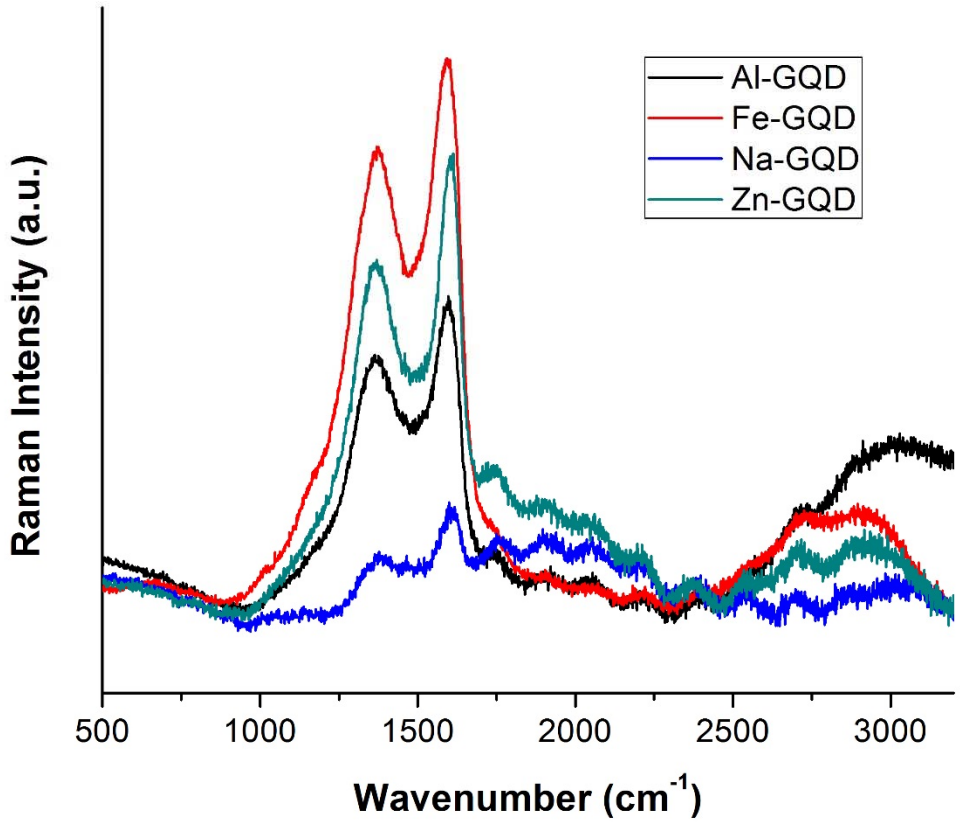

Figure S28. Experimental Raman spectra for coordination assemblies GQD for Na^{+}, Zn^{2+}, Al^{3+}, and Fe^{3+} in water for [GQD]= 10 µg/mL, [Metal]=0.5 mM, at pH 3.0.

Table S2. Cumulative electrostatic potential for the different coordination assemblies of GQD for Al^{3+}, and Fe^{3+} in water in equilibrium conformation from MD simulations. Monodentate coordination configurations were applied for Al^{3+} and bidentate coordination were employed for Fe^{3+}.

	Al-GQD (kcal)	Fe-GQD (kcal)
Dimer	-176.99	- 333.92
para- Trimer	-343.908	-607.35
meta- Trimer	-327.09	-377.11
ortho- Trimer	-295.85	-369.88

Comments: The cumulative electrostatic potentials of the coordination GQD assemblies were calculated as

$$E = \sum k_e \frac{q_1 q_2}{r} \quad (3)$$

Where k_e is the dielectric constant of the media (78.36 F/m for water), q_i is the charge for charged atoms, and r is the distance between the charged atoms. The coordinates of each atom and charges were exported from MD results at equilibrated configurations after 10 ns simulation time. The atomic charge distribution was obtained from DFT simulations.

Table S3. Detailed forcefield information of the modified Dreiding forcefield from DFT calculations.

Type	Description	Element Symbol	Van der Waals Form
Fe_3	Iron (III) ion	Fe	LJ_12_6

Bond Stretch:

F_i	F_j	Functional Form	R_o	K_o
Fe_3	O_1	Harmonic	2.006	700

Fe_3	O_R	Harmonic	2.030	700

Van der Waals Force:

Type	Position	Level1	Level2
Fe_3	All	Fe_3	X

Angle Bend:

F_i	F_j	F_k	Functional Form	T_0	K_o
X	Fe_3	X	Harmonic	90	700

Type	Position	Level1	Level2
Fe_3	End	Fe_3	X
	Center	Fe_3	X

Torsion:

Type	Position	Level1	Level2
Fe_3	End	Fe_3	X
	Center	Fe_3	X

Table S4. Atomic concentration of each elements from XPS mapping for the shungite rocks.

Sample	C [%]	O [%]	N [%]	Fe [%]	Si [%]	Na [%]	Al [%]
Shungite	69.82	20.78	2.89	0.22	4.68	0.19	1.42

References.

1. Delley, B. From molecules to solids with the DMol3 approach. *J. Chem. Phys.* **113,** 7756–7764 (2000).
2. Mattsson, A. E., Armiento, R., Schultz, P. A. & Mattsson, T. R. Nonequivalence of the generalized gradient approximations PBE and PW91. *Phys. Rev. B - Condens. Matter Mater. Phys.* **73,** (2006).
3. Russo, T. V., Martin, R. L. & Hay, P. J. Effective Core Potentials for DFT Calculations. *J. Phys. Chem.* **99,** 17085–17087 (1995).
4. Mayo, S. L., Olafson, B. D. & Goddard, W. A. DREIDING: a generic force field for molecular simulations. *J. Phys. Chem.* **94,** 8897–8909 (1990).
5. Kovalevski, V. V. & Moshnikov, I. A. TEM study of structure of graphene layers in shungite carbon. *Nanosyst. Physics, Chem. Math.* **7,** 210–213 (2016).
6. Le Guillou, C. *et al.* High resolution TEM of chondritic carbonaceous matter: Metamorphic evolution and heterogeneity. *Meteorit. Planet. Sci.* **47,** 345–362 (2012).
7. Kovalevski V.V., Safronov A.N., M. J. A. Hollow carbon microspheres and fibres produced by catalytic pyrolysis and observed in shungite rocks. *Mol. Mater.* **8,** 21–24 (1996).
8. Bazylinski, D. A., Schlezinger, D. R., Howes, B. H., Frankel, R. B. & Epstein, S. S. Occurrence and distribution of diverse populations of magnetic protists in a chemically stratified coastal salt pond. in *Chemical Geology* **169,** 319–328 (2000).
9. Mann, S., Sparks, N. H., Walker, M. M. & Kirschvink, J. L. Ultrastructure, morphology and organization of biogenic magnetite from sockeye salmon, Oncorhynchus nerka: implications for magnetoreception. *J. Exp. Biol.* **140,** 35–49 (1988).
10. Tazaki, K. Microbial formation of a halloysite-like mineral. *Clays Clay Miner.* **53,** 224–233 (2005).
11. Dodd, M. S. *et al.* Evidence for early life in Earth's oldest hydrothermal vent precipitates.

Nature **543,** 60–64 (2017).

12. Little, C. T. S., Glynn, S. E. J. & Mills, R. A. Four-hundred-and-ninety-million-year record of bacteriogenic iron oxide precipitation at sea-floor hydrothermal vents. *Geomicrobiol. J.* **21,** 415–429 (2004).
13. Papineau, D. *et al.* Ancient graphite in the Eoarchean quartz-pyroxene rocks from Akilia in southern West Greenland II: Isotopic and chemical compositions and comparison with Paleoproterozoic banded iron formations. *Geochim. Cosmochim. Acta* **74,** 5884–5905 (2010).
14. Ohtomo, Y., Kakegawa, T., Ishida, A., Nagase, T. & Rosing, M. T. Evidence for biogenic graphite in early Archaean Isua metasedimentary rocks. *Nat. Geosci.* **7,** 25–28 (2013).
15. Xia, Y. *et al.* Self-assembly of self-limiting monodisperse supraparticles from polydisperse nanoparticles. *Nat. Nanotechnol.* **6,** 580–587 (2011).
16. Pozdnyakov, I. P. *et al.* Ultrafast photophysical processes for Fe(<scp>iii</scp>)-carboxylates. *Dalt. Trans.* **43,** 17590–17595 (2014).
15. Kao, S. J., Horng, C. S., Roberts, A. P. & Liu, K. K. Carbon-sulfur-iron relationships in sedimentary rocks from southwestern Taiwan: Influence of geochemical environment on greigite and pyrrhotite formation. *Chem. Geol.* **203,** 153–168 (2004).
16. Larrasoaña, J. C. *et al.* Diagenetic formation of greigite and pyrrhotite in gas hydrate marine sedimentary systems. *Earth Planet. Sci. Lett.* **261,** 350–366 (2007).
17. Amari, S., Gallino, R., Limongi, M. & Chieffi, A. Presolar graphite from the murchison meteorite: Imprint of nucleosynthesis and grain formation. in *AIP Conference Proceedings* **847,** 311–318 (2006).
18. Falconer, K. J. The geometry of fractal sets. *Cambridge tracts Math.* **85,** xiv, 162 (1985).
19. Shen, J., Zhu, Y., Yang, X. & Li, C. Graphene quantum dots: emergent nanolights for bioimaging, sensors, catalysis and photovoltaic devices. *Chem. Commun. (Camb).* **48,** 3686–99 (2012).
20. Chazhengina, S. Y. & Kovalevski, V. V. Structural characteristics of shungite carbon subjected to contact metamorphism overprinted by greenschist-facies regional metamorphism. *Eur. J. Mineral.* **25,** 835–843 (2013).